Published in final edited form as:
Addit Manuf. 2023 January ; 62: . doi:10.1016/j.addma.2022.103381.

Characterizing light engine uniformity and its influence on liquid crystal display based vat photopolymerization printing*

Benjamin W. Caplins[a,*], **Callie I. Higgins**[a], **Thomas J. Kolibaba**[a], **Uwe Arp**[b], **C. Cameron Miller**[b], **Dianne L. Poster**[b], **Clarence J. Zarobila**[b], **Yuqin Zong**[b], **Jason P. Killgore**[a]

[a]National Institute of Standards and Technology, 325 Broadway, Boulder, CO, 80305, United States

[b]National Institute of Standards and Technology, 100 Bureau Drive, Gaithersburg, MD, 20899, United States

Abstract

Vat photopolymerization (VP) is a rapidly growing category of additive manufacturing. As VP methods mature the expectation is that the quality of printed parts will be highly reproducible. At present, detailed characterization of the light engines used in liquid crystal display (LCD)-based VP systems is lacking and so it is unclear if they are built to sufficiently tight tolerances to meet the current and/or future needs of additive manufacturing. Herein, we map the irradiance, spectral characteristics, and optical divergence of a nominally 405 nm LCD-based VP light engine. We find that there is notable variation in all of these properties as a function of position on the light engine that cause changes in extent of polymerization and surface texture. We further demonstrate through a derived photon absorption figure of merit and through printed test parts that the spatial heterogeneity observed in the light engine is significant enough to affect part fidelity. These findings help to explain several possible causes of variable part quality and also highlight the need for improved optical performance on LCD-based VP printers.

Keywords

VAT Photopolymerization; Masked Stereolithography (MSLA); Liquid Crystal Display (LCD); 3D Printing; Additive Manufacturing

1. Introduction

In the additive manufacturing process known as vat photopolymerization (VP),[1] a polymer is solidified by exposure to light in a layer-by-layer manner to build up a 3-dimensional (3D) part[1, 2]. Over the past several decades, VP has become commonplace and is capable of

---

[*] Contribution of NIST, an agency of the US government; not subject to copyright in the United States.

[*] Corresponding Author benjamin.caplins@nist.gov (Benjamin W. Caplins).

[**] Commercial equipment, instruments, or materials are identified only in order to adequately specify certain procedures. In no case does such identification imply recommendation or endorsement by the National Institute of Standards and technology, nor does it imply that the products identified are necessarily the best available for the purpose.

[1] Historically, vat photopolymerization was most commonly referred to as stereolithography, however, vat photopolymerization is a more general term and is the preferred nomenclature in ISO/ASTM 52900:2021.

creating complex parts for a diverse range of applications[3, 4, 5]. While the original basis for VP was laid out in the early 1980's and is simple in concept[6, 7], the process of VP involves a complex interplay of different topics including, but not limited to: optical physics, optical engineering, polymer/chemical formulation, photopolymerization kinetics (involving thermal, chemical, and material property gradients in time and space), and mechanical engineering (*i.e.*, implementing a printer)[8, 9, 10, 11, 12, 13]. It is a testament to the success and practicality of VP that it has achieved widespread success despite many of these topics not being thoroughly understood in the full context of a realistic/practical VP printer. A recent report from the *2019 Photopolymer Additive Manufacturing Workshop* emphasized the current challenges to advancing VP technologies and noted the importance of investigating many of the topics mentioned above[14].

The first commercially available VP printer used a laser source to initiate photopolymerization[15]. One obvious benefit of a laser-based source is that it can be easily focused to a small area with high irradiance and can be rastered across a build plane in order to cure the photopolymer in a site-specific manner. One practical difficulty with using a focused laser to cure the photopolymer is that it must be scanned extremely rapidly in a highly precise manner across a large area to cure a single layer of a 3D object. While high quality scanning systems and laser assemblies are available, they are not without cost. Additionally, in a manufacturing context, the time to cure each layer is proportional to the cross sectional area of the layer being cured, and so printing many parts on the same build plate will result in a slower print relative to printing a single part.

A potential alternative to laser-based VP printers, discussed by Hull and Kodama in the 1980's [6, 7] described a VP process where a large-area collimated light source was used to illuminate an optical mask placed close to the build plane. A significant barrier to implementing this style of printer was that the optical mask would need to be physically changed for each unique layer in a printed part and this limited the method's growth. More recent technology, however, has led to the development of programmable masks which can be changed without any physical manipulation. The two common types of programmable masks are: (1) liquid crystal displays (LCD) in either a reflective or transmissive geometry[16, 17, 18, 19, 20] and (2) digital micromirror device (DMD)[21, 22, 23, 24]. Both types of masks are commonly used as alternatives to laser-based raster VP systems and have numerous benefits and drawbacks. Without going into great detail, at present (as of 2022), LCD-based systems are generally regarded as most suitable when longer ultraviolet (UV) wavelengths (> 400 nm), lower irradiance (< 10 mW cm^{-2}), and/or larger pixel sizes (*ca*. 50 μm) are acceptable, while the DMD based systems tend to be used when shorter UV wavelengths (< 400 nm), higher irradiance (> 10 mW cm^{-2}), and/or smaller pixel sizes (< 50 μm) are necessary.

Currently, LCD-based VP printers are the most common and can range in scale from hobby level printers costing a few hundred US$ to high throughput commercial printers costing several tens of thousands of US$ [15]. One common concern in VP in commercial applications is reproducibility of the print. In this context, reproducibility can be in reference to reproducibility of a print over time (*i.e.*, on different days), and can also be reproducibility of the print over space (*i.e.*, in different places on the build plate or on different printers).

One potentially significant factor that could lead to a lack of reproducibility over time and space is the light engine that illuminates the photopolymer. A schematic of a LCD-based VP system including the most commonly employed light engine design is shown in Fig. 1. Here an array of discrete light emitting diodes (LEDs) are positioned beneath an array of lenses which serve to collimate the light prior to illuminating a transmissive LCD screen. Since LCD screens degrade rapidly under UV light (< 400 nm), most LCD-based printers operate at 405 nm.

In this manuscript we investigate the properties of a representative 405 nm light engine used in a mid-range commercially available VP printer. Specifically we investigate: (1) the effect of the LED emission spectra and its overlap with a photoinitiator spectrum, (2) the irradiance heterogeneity across the build plane, (3) the irradiance heterogeneity on the pixel length scale, and (4) the optical divergence heterogeneity across the build plane. These spatially dependent properties of the light engine are discussed in the context of how they affect the printing process with representative prints to demonstrate several of these effects. Only by having a clear understanding of the spatial heterogeneity in the current generation of light engines can future generations of printers be designed to become more reproducible. In addition, theoretical multiphysics models require more realistic descriptions of the light engines if accurate predictions are to be made[10, 11, 12, 13].

2. Methods

This manuscript focuses on characterizing the light engine for a prototypical commercially available VP printer. This printer was not chosen for any specific light engine performance characteristics. Instead, it was chosen to be representative of mid-range printers (*i.e.*, not hobbyist and not manufacturing level) that are frequently marketed for commercial (*e.g.* dental) applications. The printer uses a standard design with an aluminum build plate that is translated vertically with a stated precision of 10 μm via a lead screw drive supported by dual linear rails. The vat bottom consists of a tensioned fluorinated ethylene propylene (FEP) film of 150 μm thickness which is in direct contact with the top surface of the LCD screen. The LCD is monochromatic and has a pixel pitch of 50 μm with a useable width of *ca.* 190 mm and height of *ca.* 120 mm. The LCD is illuminated from the bottom by an array of nominally 405 nm wavelength LEDs (6 × 9 square array; 54 LEDs in total) collimated by an array of lenses (also in a 6 × 9 square array). The print files consist of a stack of PNG 8-bit images (grayscaling permitted). Layer height, layer exposure time, and other parameters are directly set on the printer touch screen.

The resin used in this manuscript is commercially known as PR48 (Colorado Photopolymer Solutions) and is considered *open source* as the formulation of the resin was released to the general public by its creator, Autodesk. PR48 is optically clear to the eye. For all prints herein, gentle washing in isopropyl alcohol (IPA) was followed by drying under a flow of dry air. No explicit post-cure (thermal or optical) was performed.

The molar absorptivity measurements shown in Fig. 2a were performed on two common photoinitiators, TPO (2,4,6-trimethylbenzoyl-diphenylphosphine oxide, *a.k.a.* Lucirin TPO or Darocur TPO) and BAPO (phenylbis (2,4,6-trimethylbenzoyl)-phosphine oxide, *a.k.a.*

Irgacure 819) which were used as received (Sigma-Aldrich). A standard 1 cm pathlength was used in a commercial UV/visible spectrometer (Thermo Fisher Scientific, Evolution 60S) using IPA as the solvent. A mass of photoinitiator was weighed out on an analytical balance and dissolved in a known volume of solvent. The concentration was selected to yield an absorbance in the linear response range of the instrument and a solvent blank spectrum was subtracted. Note that an insoluble sediment was visible for the BAPO solution indicating either photodegradation and/or impurities were present in notable quantities – thus the molar absorptivity data should likely be regarded as a lower limit.

For spectrally resolved and/or relative irradiance measurements (Fig. 2b, Fig. 3, Fig. 4b, Fig. 5a) a fiber coupled spectrometer (Avantes, AvaSpec-ULS4096CL-EVO) was used that has < 1 nm spectral resolution. The wavelength calibration was confirmed via an Hg/Ar calibration lamp and the instrument response function was measured using a NIST traceable halogen light source. A cosine corrector (Thorlabs, CCSA1) was used as the sampling optic to limit sensitivity to optical alignment/angle of incidence. Spectra were dark count subtracted and divided by the instrument response function prior to presentation to ensure the spectral lineshapes were accurate in terms of relative spectral irradiance. Spectra were either collected manually using the manufacturer’s software or collected in an automated manner using a function generator as a trigger.

For optical divergence measurements (Fig. 7) a pinhole camera was used. Here, a 200 μm pinhole (Lenox Laser, OSS-3/8-DISC-200) was placed in close proximity (< 1.5 mm) to the LCD surface and a camera (Thorlabs, CS165MU1) was placed approximately 35 mm away. Raw data from the camera was not adjusted to account for wavelength or angle of incidence responsivity. The far-field divergence patterns were converted to angular coordinates by treating the pinhole as a point source. Images were either collected manually using the manufacturer’s software or collected in an automated manner using a function generator as a trigger. The horizontal and vertical divergence data shown in Fig. 7g-h were computed by integrating each divergence pattern over the vertical and horizontal dimensions and computing the half width at half maximum of the resulting 1D profiles.

Scanning of either the fiber spectrometer probe or the pinhole camera was accomplished with a computer numerical control (CNC) machine (Genmitsu, 3018-PRO) modified to have an end effector capable of holding the necessary optics. A 2-dimensional map was collected in a line-by-line manner where for each line the optical probe was moved at a constant velocity (10 mm/s) across the LCD screen while the optical probe was triggered at a constant rate (10 Hz) using a function generator (Agilent, 33210A). Automated software was developed (Labview) to control the CNC and optical probes (spectrometer or camera). By collecting data at constant velocity (vs. pausing to collect data at each spatial location) a full 2-dimensional map could be collected with 1 mm spatial sampling in a relatively short time period (< 1 hour). As there was notable timing jitter between the start of data collection and CNC motion, a subpixel cross correlation algorithm was used to align the individual linescans to create the continuous 2-dimensional maps shown herein[25]. The spatial resolution of the mapping procedure is estimated to be < 1 mm.

Optical color microscope images of printed parts shown in Fig. 4 and Fig. 5 were collected on a commercial microscope with variable zoom, tilt, and depth composition capabilities (Keyence, VHX-1000 with VH-Z100R lens). Coaxial lighting was used and the contrast and brightness of the images was adjusted to optimize visualization.

Optical monochrome microscope images of the UV light source were collected with customized hardware. Fig. 8b-d were collected using a 10X infinity corrected objective (Mitutoyo, Plan Apo 0.28 numerical aperture) connected to a variable zoom (12.5X) optical system (Qioptiq, Optem zoom 125C) imaging onto a camera (Thorlabs, CS135MU). Fig. 8e-h were collected using the 10X objective and a 200 mm tube lens to image the UV light directly onto the camera (without the variable zoom lens). The latter arrangement ensures the numerical aperture (NA) of the optical system is significantly larger than the illumination NA – *i.e.*, light rays are not being clipped in the optical system.

Laser scanning confocal microscopy topography data shown in Fig. 9 was collected on a commercial instrument (Keyence, VK-X1000) utilizing a 50X objective. The height data was calculated automatically in the instrument software by locating the maxima of the depth-response curve at each pixel[26] – this allows for finding the air/polymer interface even for weakly scattering (*e.g.* transparent samples). Height data was cropped and flattened to a plane using open source software (Gwyddion).

3. Results

Most commercially available VP resins are based on a photoinitiated radical chain growth mechanism[8]. Here, a photon is absorbed by a photoinitiator which generates radicals which starts a photopolymerization reaction which ultimately is intended to generate a solid. As the initiation step relies on photon absorption, the optical properties of the photoinitiator and the light source dictate the rate of radical generation and thus photoinitiation. Specifically, the overlap of the absorption spectrum of the photoinitiator species and the spectral irradiance of the light source dictate the radical generation rate[27].

Fig. 2 shows the molar absorptivity plot for two common photoinitiators, TPO and BAPO. Both photoinitiators show strong absorption from 350 nm to 400 nm with a tailing off of the absorption in the around 420 nm. These spectra are in reasonable agreement with published data[28, 29], though we note that there is surprisingly large variability in the BAPO molar absorptivity reported in the literature – values can be found ranging from *ca.* 300 $\mathrm{cm^{-1}mol^{-1}L}$ at 370 nm[30] to *ca.* 1400 $\mathrm{cm^{-1}mol^{-1}L}$ at 370 nm[29], though literature molar absorptivity values tend to be closer to 1000 $\mathrm{cm^{-1}mol^{-1}L}$ at 370 nm, in agreement with our data[31, 32]. Most literature data on TPO is generally consistent[30, 29, 33]. While the cause of this variability in the BAPO measurements is unknown it has been noted previously[29].

Two things are immediately obvious when looking at the molar absorptivity data. First, at the same molar concentration BAPO absorbs light more strongly than TPO. Second, at the 405 nm wavelength used by most LCD-based printers, the magnitude of the slope of the absorption curve is nearly maximal. A large slope in the photon absorption near 405 nm implies that the photon absorption rate (*i.e.*, photoinitiation rate) will be sensitive to the light source center wavelength and spectral width. In contrast, a light source centered between 365 nm and 395 nm would be relatively insensitive to small variations in the spectral properties of the light source. Unfortunately, since LCD screens degrade more rapidly as the illumination is blue-shifted, most LCDs are illuminated with 405 nm light sources.

Fig. 2b shows three arbitrarily chosen commercially available LED light sources present in our laboratory that are nominally 405 nm. One of these LED sources is a 3D printer light engine, one source is a microscopy light, and the other source is a bare LED. Despite being nominally 405 nm LEDs, there is considerable variation in the spectral properties. Here, LED ‘A’ is 5 nm blue shifted of LED ‘C’, and LED ‘A’ is 4.5 nm wider than LED ‘B’. This type of spectral heterogeneity is expected during LED manufacturing. In fact, as manufactured LEDs are typically tested for their electrical and/or optical properties and placed into bins based on the measured values. In the UV, LEDs sold with 5 nm wide wavelength bins would be considered high-quality with larger bins (*e.g.* 10 nm) being common[34]. The spectral width (fwhm) of LEDs can vary as well, but is generally not explicitly bounded with max/min values on a datasheet – instead just a typical value is provided. In summary, even for nominally identical LEDs purchased at the same time from the same manufacturer, a 5 nm to 10 nm variation of center wavelength cannot be ruled out. Additionally, variation in the spectral width on the order of 5 nm to 10 nm is also possible.

In order to understand how the variation in the optical parameters of the light source can impact the radical generation rate we need a figure of merit (FoM). Here, we choose to use a FoM proportional to the rate of change of the irradiance evaluated in the limit of an optically thin sample (*i.e.*, the front face of the sample). The irradiance can be written:

$$I(z) = I_0 \int_{\lambda_{min}}^{\lambda_{max}} S(\lambda) \cdot \exp(-\alpha(\lambda) \cdot z)\, d\lambda \tag{1}$$

where I_0 is the total irradiance, $S(\lambda)$ is the lineshape function which is normalized to have an integral of 1, $\alpha(\lambda)$ is the absorption coefficient, z is the distance from the sample surface, and λ is integrated over the relevant spectral range. The absorption coefficient can be expressed in terms of the molar absorptivity and molar concentration, $\alpha(\lambda) = \ln(10)\epsilon(\lambda)[C]$. Then the rate of change of the irradiance evaluated at $z = 0$ is:

$$\frac{dI}{dz}\bigg|_{z=0} = -I_0 \ln(10)\,[C] \int_{\lambda_{min}}^{\lambda_{max}} S(\lambda) \cdot \epsilon(\lambda)\, d\lambda \tag{2}$$

Normalizing this quantity to the negative of the initial irradiance and molar concentration of the photoinitiator yields a useful FoM for photon absorption efficiency which we denote as Σ:

$$\Sigma = \int_{\lambda_{min}}^{\lambda_{max}} S(\lambda) \cdot \epsilon(\lambda)\, d\lambda \tag{3}$$

Σ has the same units as $\epsilon(\lambda)$ (*i.e.*, $\mathrm{cm^{-1}mol^{-1}L}$) and can be interpreted as an average of the molar absorptivity weighted by the incident light spectrum. Importantly, we note that this FoM is not intended to directly model an actual resin as it does not incorporate such factors as photobleaching or additional photoabsorbers. Instead, this FoM was designed to demonstrate the relative importance of spectral irradiance on photoinitiation.

In Fig 2c-e the FoM, Σ, is plotted for different theoretical test light sources. In these panels Σ is normalized to the value of Σ for the BAPO/LED 'C' combination. Fig 2c shows the linear dependence of Σ on the irradiance, where the difference in slopes between TPO and BAPO is just related to the different magnitudes of molar absorptivity. Fig 2d shows the nonlinear dependence of Σ on the center wavelength of the lineshape function – *i.e.*, taking the overlap of the TPO and BAPO molar absorptivity and the lineshape function of LED 'C' which is shifted to higher or lower wavelengths by $\Delta\lambda$. These curves are effectively the convolution of the LED 'C' spectrum with the molar absorptivities. Fig 2e shows the roughly linear dependence of Σ on the linewidth – i.e., taking the overlap of the TPO and BAPO molar absorptivity and the lineshape function of LED 'C' which has been linearly stretched or compressed to have a larger or smaller fwhm.

We can look at the relative variation of these curves as a function of each parameter, denoted $\Delta\Sigma/\Sigma$, to understand more generally how variation of these parameters (I_0, center wavelength, and linewidth) affects the radical generation rate. In Fig. 2c we see that the sensitivity of the radical generation rate to irradiance is linear as expected – *i.e.*, a 10 % variation in the irradiance leads to a 10 % variation in Σ. In Fig. 2d we see that for every 1 nm that the light source is shifted Σ changes by 5 % for BAPO and 12 % for TPO. Thus, a 5 nm shift – which we measured in Fig. 2b and may also be expected due to the way LEDs are binned – could result in up to a 25 % change for BAPO or 60 % change for TPO. This strongly suggests that printer light engines based on 405 nm LEDs should pay particular attention to maintaining wavelength homogeneity to a level beyond what is guaranteed by the LED manufacturer. Finally, in Fig. 2e we see that for every 1 nm that the light source fwhm is changed, Σ changes by 0.5 % for BAPO and 3.3 % for TPO. In this case, the sensitivity of Σ to changes in fwhm is not necessarily negligible – i.e., changes on the order of 10 % could occur – but is secondary to the center wavelength of the light source.

The previous discussion sought to understand how variations in light source parameters affect the radical generation/photoinitiation rate using a randomly chosen LED as an example, but what is more interesting is how these light source parameters may vary across an actual light engine used in a VP printer. To measure these spectral properties in a spatially resolved manner a fiber spectrometer was rastered across the print plane above the LCD as shown in Fig. 3a. At each position the relative irradiance, peak centroid, and fwhm was extracted from the spectra and plotted in 3b-d. It is immediately clear that the light source is constructed in such a manner that a square pattern arises. Each square represents the light output from a single LED imaged through a lens. This is most obvious when inspecting the centroid map where the region illuminated by each LED can be clearly distinguished. In the irradiance map the intense horizontal and vertical features are due to overlapping illumination at the edge of each LED's illumination area.

To understand how the spatially varying irradiance, centroid, and peak width parameters could affect a radical generation rate the range of values in each map should be inspected. For the irradiance map, the irradiance varies almost a factor of 3 between the brightest and darkest regions (2.00 arb. units to 0.68 arb. units). For the centroid map, the wavelength varies by 2.8 nm (409.7 nm to 412.5 nm). And for the peak width map the fwhm varies by around 1.5 nm (15.5 nm to 17.0 nm). If we consider what these variations do to the FoM (Fig. 2c-e), then they change the rate of photon absorption for a TPO-based resin by 290 %, 34 %, and 5 % respectively for the irradiance, center wavelength, and peak width heterogeneity. In this case, it is clear that the irradiance heterogeneity will dominate the variation in photoinitiation rate.

In order to visualize how this light engine heterogeneity can impact a printed part, ‘inside corner’ test parts were printed and imaged under an optical microscope in Fig. 4 (see Supplementary Materials for part specifications). Specifically, two intercalated grids on test parts were printed centered at the regions of higher irradiance and lower irradiance. Inspection of the inside edge where the two square pillars are designed to touch shows observable differences between the two grid locations. The higher irradiance locations show a joining of the two squares for the full height (Fig. 4d). Additionally, the surface texture of the final layer (last in contact with the FEP) is quite smooth (Fig. 4f). In contrast, the lower irradiance locations show little to no joining of the two squares which results in notable lateral corner separation in the final layer (Fig. 4g). Also, the final layer surface appears quite textured (Fig. 4i). While there was some small variation in the appearance of the 68 test parts, the features seen in Fig. 4 are representative – the most common difference was how many layers were connected with filaments prior to full separation in the lower irradiance test parts.

We hypothesized that the difference in irradiance between the two sites caused the observed variations in prints. To test this, a grayscale digital mask (8 bit) was constructed for the LCD such that the irradiance map would be more uniform. The irradiance map was then remeasured in the same manner as in Fig. 3a-b and shown in Fig. 5a. Since grayscaling the LCD can only lower the irradiance and not increase it, the average irradiance was lower, but the relative irradiance variation was reduced dramatically. With this improved uniformity, the same ‘inside corner’ test parts were printed using a longer exposure time to partially counteract the lowered overall irradiance. These prints were imaged under an optical microscope in Fig. 5b-e. Notably, the inside corners now have a similar amount of separation (Fig. 5b,d) supporting the hypothesis that the variation in the prints was driven by the spatial variation in irradiance of the light engine. To further support this hypothesis, the corner-to-corner separation distance was measured for all 68 test parts in both the uncorrected and grayscale corrected data sets and is shown in Fig. 6. The corner-to-corner distance distributions were non-overlapping in the uncorrected prints, but strongly overlapping in the grayscale uniformity corrected prints. The obvious differences in final surface texture (Fig. 5c,e), however, appear unchanged with the more uniform irradiance suggesting the surface texture arises from a different mechanism.

LCD pixels are known to have a fill factor less than 1 due to the need for electrical component layers, and thus if the divergence of the light source is not sufficient, then the illuminated area pixel may be less than the pixel pitch would require (*i.e.*, 50 μm × 50 μm square region). This incomplete illumination could potentially give rise to increased surface texture[35]. Specifically, to account for the variation seen in the ‘inside corner’ test parts the divergence would need to vary across the build plate in a significant manner. To test this we rastered a pinhole camera across the build plate while collecting the images associated with the light source divergence (Fig. 7a). The total integrated signal on the camera shown in Fig. 7b is approximately the same as the irradiance as measured with the fiber spectrometer probe. In Fig. 7c-f we show the far field divergence patterns associated with the the four locations labeled in Fig. 7b as i-iv. Fig. 7d shows the pattern collected coaxial with a single LED/lens pair and it can be roughly interpreted as both a magnified image of the LED emitter, or more importantly, the angular distribution of light transmitted through the pinhole at the LCD screen. With this latter interpretation we can see that at location ii the light has a divergence half angle of approximately 1°. In contrast, Fig. 7c shows location i has a divergence half angle of closer to 3°, which can be explained by noting that there appear to be four different LED emitters contributing. Similarly, Fig. 7e-f show asymmetric divergence characteristics due to the contribution of either two horizontally or vertically neighboring LED emitters. As a way of visualizing the data more succinctly, Fig. 7g-h show the vertical and horizontal divergence half angle across the build plate – here the overlap between neighboring LEDs is clearly visible. This overlap between LED illumination simultaneously explains the non-uniform irradiance and the nonuniform divergence. Importantly, when the irradiance map was flattened with a grayscale mask, the nonuniform divergence remains.

Looking more closely at the effect of this nonuniform divergence requires imaging the irradiance on subpixel length scales. Here we use a microscope objective to magnify the light onto a camera (Fig. 8a); the entire assembly is placed on a translation stage so the focal plane can be precisely shifted. When the LCD pixels are brought into focus, it is apparent that the fill factor for these LCD pixels is much less than 100 % and is approximately 50 %. When the focal plane is shifted to the where the top surface of the FEP would normally be (*i.e.*, where the resin would begin) the pixels blur out significantly due to the source divergence and scattering[10, 35]. Fig. 8e-h show the irradiance distributions for the four locations called out in Fig. 7b (i-iv). These data are consistent with the interpretation that the low fill factor of the LCD pixels combines with the nonuniform divergence of the light engine to yield pixels that are frequently underfilled at the print plane and can cause the incomplete polymerization of the printed pixels (*i.e.*, 50 μm × 50 μm square region) observed as increased surface texture of the ‘inside corner’ test parts.

To emphasize that these optical measurements really do have direct relevance to the print process we carry out two further experiments. First, we print test parts that are completely flat until the final layer which has only 25 % of the pixels turned on. Mapping the topography of this final layer on a laser scanning confocal microscope permits us to directly visualize how the projected light distribution through a single pixel manifests in the print process. Fig. 9a-d shows the topography maps collected from the same locations called out in Fig. 7b (i-iv). Here we see that spatial size and symmetry of the printed pixels corresponds well with the divergence data (Fig. 7c-f) and the pixel scale irradiance data (Fig. 8e-h).

A final test part was printed where 100 % of the pixels were turned on – here, the naive expectation of a homogenous light source would suggest that the test print has a flat surface. Fig. 9e-h shows the topography data collected from the same locations called out in Fig. 7b (i-iv). Comparing the optical data in Fig. 8e-h to the height data in Fig. 9e-h confirms that the irradiance at the single pixel length has a direct impact on the print process and can reasonably explain the surface texture observed in the 'inside corner' test parts. For all prints in Fig. 9, the irradiance was made to be uniform with the gray scale mask mentioned previously such that the differences in the topography cannot be attributed to the larger length scale differences in irradiance observed on the native printer.

4. Discussion

To summarize the previous observations: the commercially available LCD-based VP light engine under study deviates from an ideal light engine in several important ways and this directly impacts the print process.

The first major concern of LCD-based light engines arises from the fact that there are multiple emitters (54 emitters for the light engine under study). Thus, any heterogeneity in these LEDs in terms of irradiance, center wavelength, or linewidth can yield notable spatial differences in the photon absorption rate and subsequent photoinitiated chemistry. The spectral properties are of especially a concern when the overlap of the light source spectrum and the photoinitiator absorption are poor, which is precisely the case for most LED-based light engines which operate at > 400 nm for device lifetime/reliability reasons. As a point of reference, it is common for printer manufacturers to suggest optimizing the exposure time for a resin using steps of approximately 5 % to 10 % of the total exposure time. For the light engine under study, the observed variations in spectral properties can easily account for $\gg 5$ % variations in photon absorption (Fig. 2 and Fig. 3) and so are expected to be of practical relevance for printing parts with fine details. Though not discussed herein, compounding this is the fact that the degree of conversion as a function of depth is also a sensitive function of the light source properties[31].

The second major concern of LCD-based light engines arises from the fact that the photons from all the emitters must be combined into a single light source incident on the LCD. For the light engine under study, overlap of the light emitted from separate LEDs caused spatial variation in the irradiance and the divergence properties of the light transmitting the LCD screen. The observed irradiance nonuniformity across the light engine (Fig. 3) was enough to lead to obvious changes in the dimensions for simple printed parts (Fig. 4). And even after using a grayscale correction to remove most of the irradiance nonuniformity, the observed divergence nonuniformity across the light engine (Fig. 7, Fig. 8) was enough to lead to changes in the surface texture for printed parts (Fig. 5, Fig. 9) because the light is not divergent enough to fully illuminate the voxel after transmitting through the LCD mask (Fig. 8)[35].

This work suggests a number of improvements are possible to LCD-based VP light engines. First, we note that the irradiance nonuniformity is what dominates the variation in photon absorption rate across the light engine and so improving the optics in order to minimize this irradiance nonuniformity is of chief importance. In addition, for irradiance nonuniformity that cannot be removed via optical engineering, methods to quickly characterize and create digital masks to correct the nonuniformity are needed. For inspiration the community can undoubtedly look to the more mature flat panel display characterization methods already established[36]. Second, the spectral homogeneity of the LED emitters is also of nontrivial importance, and so performing in-house testing of manufacturer supplied LEDs in order to place them into bins with tighter, more application specific tolerances should further improve the photon absorption uniformity and print reproducibility. Finally, we emphasize that care should be taken to ensure that the divergence properties of the light are not neglected when designing light engines, as this can directly impact surface texture.

Herein, we characterized a prototypical LCD-based VP light engine in detail ranging from the subpixel to build plate lengthscales. While different model light engines from the same or different manufacturers will undoubtedly differ quantitatively, we expect the relative importance of the various optical properties to be conserved due to the fact that most manufacturers utilize similar light engine designs. Understanding and removing the spatial nonuniformities of these optical properties should allow for more reproducible 3D printing. Additionally, recent theoretical modeling has begun to incorporate more realistic pixel illumination sources, but this work demonstrates that these model pixel sources – while a great step forward from binary square sources with 100 % fill factor – are probably still too simplistic. Notably, combining advanced light engine characterization with appropriate modeling could allow for optimized printing via gray level control[37] thus reducing the influence of light engine on the printed parts.

Finally, we note that VP printers based on laser raster or digital micromirror devices will have distinct optical concerns which this work does not address.

5. Conclusions

Herein we investigated the optical properties of a LCD-based VP light engine in greater detail than has been previously explored. An emphasis was placed on understanding how these optical properties correlate to the photon absorption and thus printing process. We found that for LCD-based printers (nominally at 405 nm) the variation in spectral properties (center wavelength and lineshape) of the LEDs can significantly impact the photon absorption/photoinitation process. Additionally, the optical system guiding the light from the LEDs to the LCD caused spatial variation in irradiance causing geometrical variation in the as-printed parts. Finally, the optical system also caused spatial variation in the divergence of the light transmitted through each LCD pixel, which caused heterogeneity of the surface texture of printed parts. These experiments suggest improvements in LCD-based VP light engines are necessary for better print reproducibility while also informing how these improvements can be made. Long term, light engines with improved optical properties will allow for more reproducible VP printing with less concern for build plate heterogeneity.

Supplementary Material

Refer to Web version on PubMed Central for supplementary material.

Acknowledgments

We thank Ryan White (NIST) for help with the optical microscopy instrumentation. We acknowledge the MIMIC facility at CU Boulder (RRID:SCR_019307) for the use of the laser scanning confocal microscope.

References

[1]. Bourell DL, Perspectives on Additive Manufacturing, Annual Review of Materials Research 46 (2016) 1–18. doi: 10.1146/annurev-matsci-070115-031606.

[2]. Zhang F, Zhu L, Li Z, Wang S, Shi J, Tang W, Li N, Yang J, The recent development of vat photopolymerization: A review, Additive Manufacturing 48 (2021) 102423. doi:10.1016/j.addma.2021.102423. URL https://linkinghub.elsevier.com/retrieve/pii/S2214860421005753

[3]. Melchels FP, Feijen J, Grijpma DW, A review on stereolithography and its applications in biomedical engineering, Biomaterials 31 (24) (2010) 6121–6130. doi:10.1016/j.biomaterials.2010.04.050. URL 10.1016/j.biomaterials.2010.04.050 [PubMed: 20478613]

[4]. Zheng X, Lee H, Weisgraber TH, Shusteff M, DeOtte J, Duoss EB, Kuntz JD, Biener MM, Ge Q, Jackson JA, Kucheyev SO, Fang NX, Spadaccini CM, Ultralight, ultrastiff mechanical metamaterials, Science 344 (6190) (2014) 1373–1377. doi:10.1126/science.1252291. [PubMed: 24948733]

[5]. Chen D, Zheng X, Multi-material Additive Manufacturing of Metamaterials with Giant, Tailorable Negative Poisson's Ratios, Scientific Reports 8 (1) (2018) 9139. doi:10.1038/s41598-018-26980-7. URL http://www.nature.com/articles/s41598-018-26980-7 [PubMed: 29904093]

[6]. Hull CW, Apparatus for Production of Three-Dimensonal Objects by Stereolithography (1986).

[7]. Kodama H, Automatic method for fabricating a three-dimensional plastic model with photo-hardening polymer, Review of Scientific Instruments 52 (11) (1981) 1770–1773. doi:10.1063/1.1136492. URL http://aip.scitation.org/doi/10.1063/1.1136492

[8]. Decker C, Photoinitiated crosslinking polymerisation, Progress in Polymer Science 21 (4) (1996) 593–650. doi:10.1016/0079-6700(95)00027-5. URL https://linkinghub.elsevier.com/retrieve/pii/0079670095000275

[9]. Decker C, Decker D, Morel F, Light Intensity and Temperature Effect in Photoinitiated Polymerization, 1997, pp. 63–80. doi:10.1021/bk-1997-0673.ch006. URL https://pubs.acs.org/doi/abs/10.1021/bk-1997-0673.ch006

[10]. Emami MM, Rosen DW, Modeling of light field effect in deep vat polymerization for grayscale lithography application, Additive Manufacturing 36 (2020) 101595. doi:10.1016/j.addma.2020.101595. URL https://linkinghub.elsevier.com/retrieve/pii/S2214860420309672

[11]. Classens K, Hafkamp T, Westbeek S, Remmers JJ, Weiland S, Multiphysical modeling and optimal control of material properties for photopolymerization processes, Additive Manufacturing 38 (2021) 101520. doi:10.1016/j.addma.2020.101520. URL https://linkinghub.elsevier.com/retrieve/pii/S2214860420308927

[12]. Westbeek S, Remmers J, van Dommelen J, Maalderink H, Geers M, Prediction of the deformed geometry of vat photo-polymerized components using a multi-physical modeling framework, Additive Manufacturing 40 (2021) 101922. doi:10.1016/j.addma.2021.101922. URL https://linkinghub.elsevier.com/retrieve/pii/S2214860421000877

[13]. Montgomery SM, Hamel CM, Skovran J, Qi HJ, A reaction–diffusion model for grayscale digital light processing 3D printing, Extreme Mechanics Letters 53 (2022) 101714. doi:10.1016/j.eml.2022.101714. URL https://linkinghub.elsevier.com/retrieve/pii/S2352431622000645

[14]. Higgins C, Killgore J, Poster D, Report from the Photopolymer Additive Manufacturing Workshop: Roadmapping a Future for Stereolithography, Inkjet, and Beyond, Tech. rep., National Institute of Standards and Technology, Gaithersburg, MD (jan

2021). doi:10.6028/NIST.SP.1500-17. URL https://nvlpubs.nist.gov/nistpubs/SpecialPublications/NIST.SP.1500-17.pdf

[15]. Wohlers T, Gornet T, History of Additive Manufacturing 2014, Tech. rep (2014).

[16]. Ventura SC, Narang SC, Sharma S, Stotts J, Liu C, Liu S, Ho L-H, Annavajjula D, Lombardo S, Hardy A, Mangaudis M, Chen E, Groseclose L, A New SFF Process for Functional Ceramic Components, in: International Solid Freeform Fabrication Symposium, 1996, pp. 327–334.

[17]. Bertsch A, Jézéquel J, André J, Study of the spatial resolution of a new 3D microfabrication process: the microstereophotolithography using a dynamic mask-generator technique, Journal of Photochemistry and Photobiology A: Chemistry 107 (1–3) (1997) 275–281. doi:10.1016/S1010-6030(96)04585-6. URL https://linkinghub.elsevier.com/retrieve/pii/S1010603096045856

[18]. Bertsch A, Zissi S, Jézéquel JY, Corbel S, André JC, Microstereophotolithography using a liquid crystal display as dynamic mask-generator, Microsystem Technologies 3 (2) (1997) 42–47. doi:10.1007/s005420050053. URL http://link.springer.com/10.1007/s005420050053

[19]. Young JS, Fox SR, Anseth KS, A Novel Device for Producing Three-Dimensional Objects, Journal of Manufacturing Science and Engineering 121 (3) (1999) 474–477. doi:10.1115/1.2832705. URL https://asmedigitalcollection.asme.org/manufacturingscience/article/121/3/474/434521/A-Novel-Device-for-Producing-ThreeDimensional

[20]. Zheng X, Deotte J, Alonso MP, Farquar GR, Weisgraber TH, Gemberling S, Lee H, Fang N, Spadaccini CM, Design and optimization of a light-emitting diode projection micro-stereolithography three-dimensional manufacturing system, Review of Scientific Instruments 83 (12) (2012) 125001. doi:10.1063/1.4769050.URL http://aip.scitation.org/doi/10.1063/1.4769050 [PubMed: 23278017]

[21]. Sampsell JB, Digital micromirror device and its application to projection displays, Journal of Vacuum Science and Technology B: Microelectronics and Nanometer Structures 12 (6) (1994) 3242. doi:10.1116/1.587506. URL http://scitation.aip.org/content/avs/journal/jvstb/12/6/10.1116/1.587506

[22]. Akahane T, Takahashi K, Non-Scanning Rapid Prototyping System using a Digital Micromirror Device, IEEJ Transactions on Sensors and Micromachines 121 (5) (2001) 275–280. doi:10.1541/ieejsmas.121.275. URL http://www.jstage.jst.go.jp/article/ieejsmas1995/121/5/121_5_275/_article

[23]. Bertsch A, Bernhard P, Renaud P, Microstereolithography: concepts and applications, in: ETFA 8th International Conference on Emerging Technologies and Factory Automation. Proceedings, Vol. 2, IEEE, 2001, pp. 289–298. doi: 10.1109/ETFA.2001.997697. URL http://ieeexplore.ieee.org/document/997697/

[24]. Sun C, Fang N, Wu D, Zhang X, Projection micro-stereolithography using digital micro-mirror dynamic mask, Sensors and Actuators A: Physical 121 (1) (2005) 113–120. doi:10.1016/j.sna.2004.12.011. URL https://linkinghub.elsevier.com/retrieve/pii/S0924424704008672

[25]. Guizar-Sicairos M, Thurman ST, Fienup JR, Efficient subpixel image registration algorithms, Optics Letters 33 (2) (2008) 156. doi:10.1364/OL.33.000156. URL https://opg.optica.org/abstract.cfm?URI=ol-33-2-156 [PubMed: 18197224]

[26]. Udupa G, Singaperumal M, Sirohi RS, Kothiyal MP, Characterization of surface topography by confocal microscopy: I. Principles and the measurement system, Measurement Science and Technology 11 (3) (2000) 305–314. doi:10.1088/0957-0233/11/3/320. URL https://iopscience.iop.org/article/10.1088/0957-0233/11/3/320

[27]. Stahl F, Light-emitting diode (LED) polymerisation of dental composites: flexural properties and polymerisation potential, Biomaterials 21 (13) (2000) 1379–1385. doi:10.1016/S0142-9612(00)00029-6. URL https://linkinghub.elsevier.com/retrieve/pii/S0142961200000296 [PubMed: 10850932]

[28]. Ciba Specialty Chemicals, Photoinitiators for UV Curing, Tech. rep (2003). URL https://gnusha.org/$\sim$nmz787/mems/unorganized/PhotoinitiatorsforUVcuring.pdf

[29]. Rundlett B, Photoinitiator Selection, in: Radtech Technology Conference, 2012. URL https://www.radtech.org/proceedings/2012/papers/end-user-presentations/LED/DSM_Rundlett_LED.pdf

[30]. Neumann MG, Miranda WG, Schmitt CC, Rueggeberg FA, Correa IC, Molar extinction coefficients and the photon absorption efficiency of dental photoinitiators and light curing

units, Journal of Dentistry 33 (6) (2005) 525–532. doi:10.1016/j.jdent.2004.11.013. URL https://linkinghub.elsevier.com/retrieve/pii/S0300571205000072 [PubMed: 15935273]

[31]. Gong H, Bickham BP, Woolley AT, Nordin GP, Custom 3D printer and resin for 18 μm × 20 μm microfluidic flow channels, Lab on a Chip 17 (17) (2017) 2899–2909. doi:10.1039/C7LC00644F. URL http://xlink.rsc.org/?DOI=C7LC00644F [PubMed: 28726927]

[32]. Dietlin C, Trinh TT, Schweizer S, Graff B, Morlet-Savary F, Noirot P-A, Lalevée J, New Phosphine Oxides as High Performance Near- UV Type I Photoinitiators of Radical Polymerization, Molecules 25 (7) (2020) 1671. doi: 10.3390/molecules25071671. URL https://www.mdpi.com/1420-3049/25/7/1671 [PubMed: 32260383]

[33]. Miletic V, Santini A, Optimizing the concentration of 2,4,6-trimethylbenzoyldiphenylphosphine oxide initiator in composite resins in relation to monomer conversion, Dental Materials Journal 31 (5) (2012) 717–723. doi:10.4012/dmj.2012-064. URL https://www.jstage.jst.go.jp/article/dmj/31/5/31_2012-064/_article [PubMed: 23037832]

[34]. Heathcote J, UV-LED Overview Part I - Operation and Measurement, Tech. Rep August (2010). URL https://radtech.org/magazinearchives/Publications/RadTechReport/jul-aug-2010/UV-LEDBasicsPartI-OperationandMeasurement.pdf

[35]. Shan Y, Krishnakumar A, Qin Z, Mao H, Reducing lateral stair-stepping defects in liquid crystal display-based vat photopolymerization by defocusing the image pattern, Additive Manufacturing 52 (2022) 102653. doi:10.1016/j.addma.2022.102653. URL https://linkinghub.elsevier.com/retrieve/pii/S2214860422000598

[36]. Ming W, Zhang S, Liu X, Liu K, Yuan J, Xie Z, Sun P, Guo X, Survey of Mura Defect Detection in Liquid Crystal Displays Based on Machine Vision, Crystals 11 (12) (2021) 1444. doi:10.3390/cryst11121444. URL https://www.mdpi.com/2073-4352/11/12/1444

[37]. Guven E, Karpat Y, Cakmakci M, Improving the dimensional accuracy of micro parts 3D printed with projection-based continuous vat photopolymerization using a model-based grayscale optimization method, Additive Manufacturing 57 (February) (2022) 102954. doi:10.1016/j.addma.2022.102954. URL 10.1016/j.addma.2022.102954https://linkinghub.elsevier.com/retrieve/pii/S2214860422003487

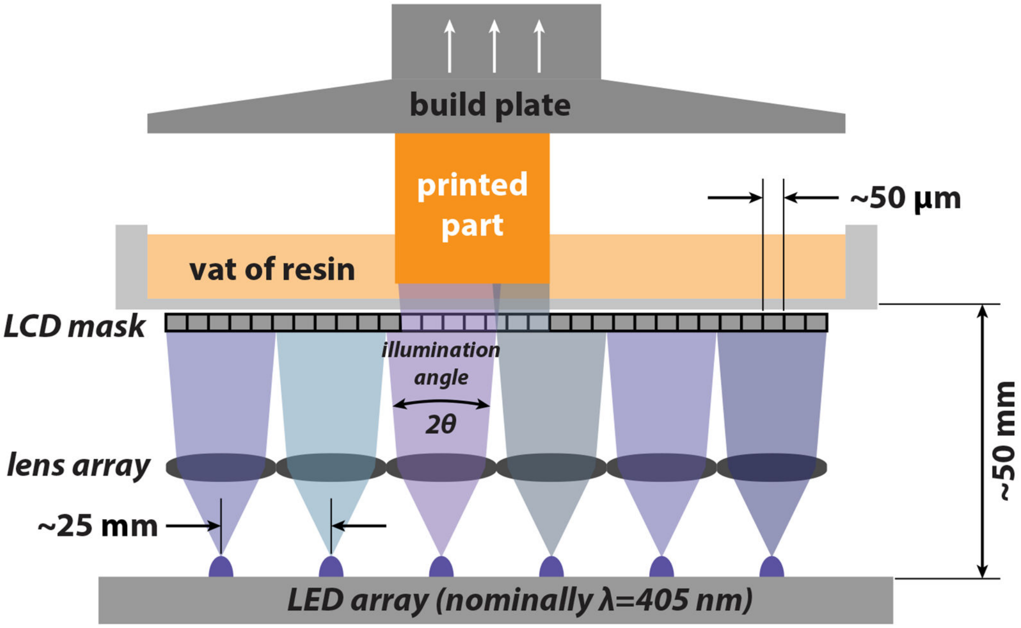

Figure 1:

A schematic of a LCD-based vat photopolymerization (VP) printer. The spatial extent of the photopolymerization in each layer is controlled by a programmable LCD mask. The LCD is illuminated by an array of light emitting diodes (LEDs) which are collimated by an array of lenses. In a typical LCD-based VP system the LEDs are spaced out by *ca.* 25 mm, and have a nominal emission wavelength of 405 nm. The LCD pixel pitch is *ca.* 50 µm and the total optical pathlength between the LED and the resin is on the order of 50 mm. Notably, because an array of LEDs and lenses are used to illuminate the resin, any variation in LED emission (intensity and/or spectrum) is transferred to the build plane. In addition, individual pixels may be illuminated differently depending on where they are positioned with respect to the LEDs/lenses.

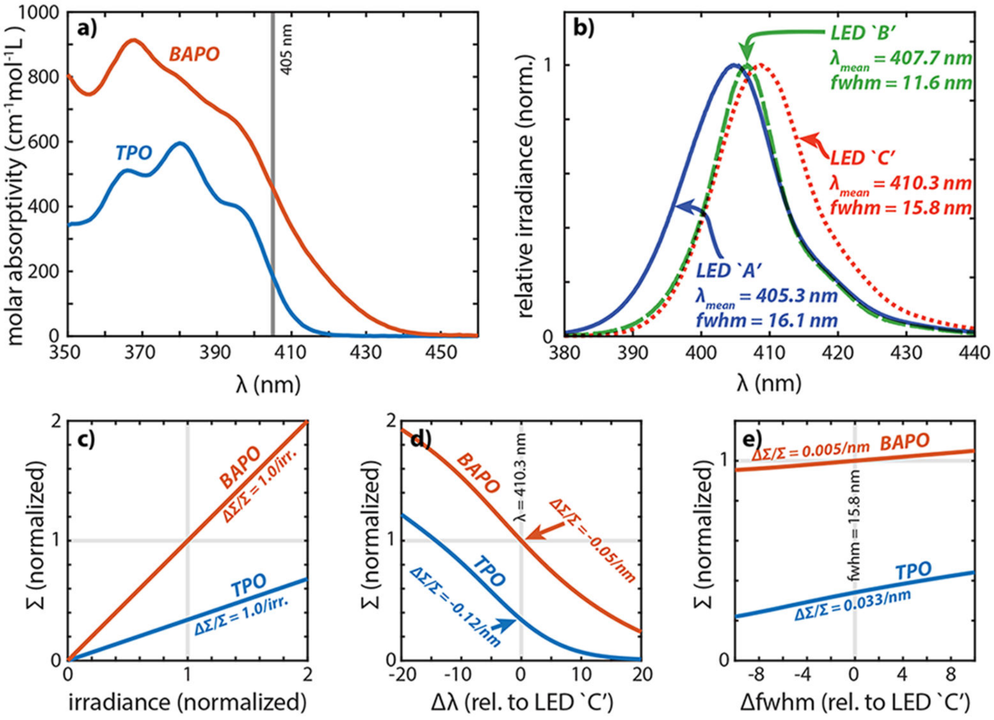

Figure 2:

(a) Molar absorptivity for two common photoinitiators in IPA. Note the BAPO solution had insoluble sediment observable and is thus considered to be a lower bound to the true values. (b) The spectrum of three randomly chosen nominally 405 nm LEDs. (c) The overlap integral (Σ) between the LED ‘C’ light source and the molar absorptivity which is used as a figure of merit (FoM) for photon absorption. (d) The overlap integral between the LED ‘C’ lineshape and the molar absorptivity for a range of center wavelengths (relative to the LED ‘C’ spectrum center wavelength of λ = 410.3 nm). (e) The overlap integral between the LED ‘C’ lineshape and the molar absorptivity for a range of linewidths (relative to the LED ‘C’ linewidth which has a full width at half maximum of 15.8 nm). The overlap integrals are all normalized to the as measured BAPO/LED ‘C’ value. Relative sensitivity of the FoM to irradiance, center wavelength, and linewidth are specified on each plot as ΔΣ/Σ.

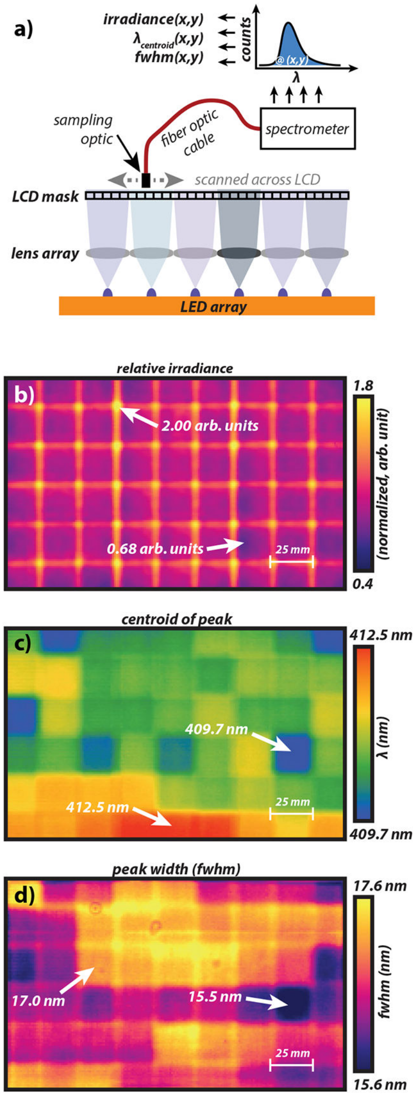

Figure 3:

(a) Measurement schematic for spatially mapping the emission of the UV light transmitted through the LCD. A fiber probe with a cosine corrector sampling optic is rastered across the LCD surface while collecting spectra. (b) A map of the total irradiance (integration between 375 nm and 475 nm) normalized to the mean irradiance. Here all LCD pixels are fully on. The total field of view is 120 mm × 190 mm. (c) A map of the centroid of the spectra (integration window between 375 nm and 475 nm). (d) A map of the peak width expressed as full width at half maximum (fwhm).

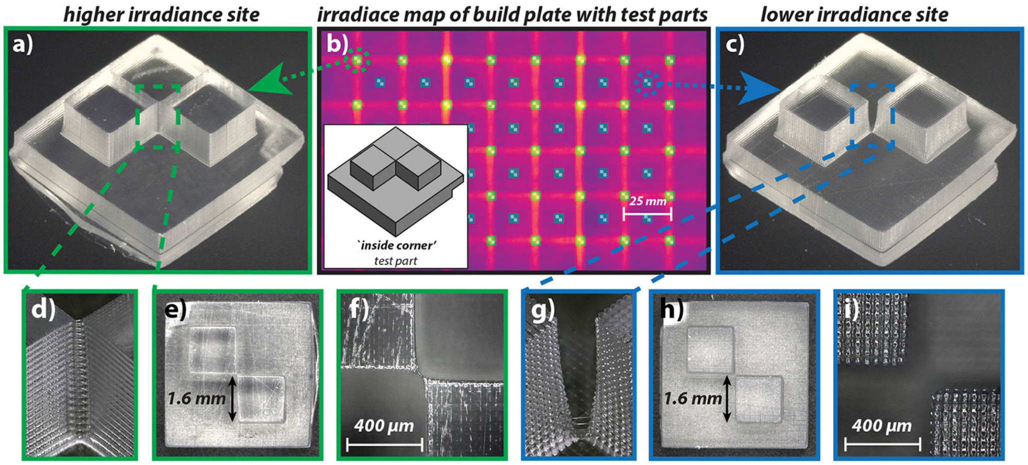

Figure 4:

(b) A diagram of where 68 different ‘inside corner’ test artifacts (see inset) were placed relative to the irradiance map. Two intercalated grids are present: one set of sites (5 × 8 grid) is located at the highest irradiance areas where vertical and horizontal linear features cross, and one set of sites (4 × 7 grid) is located at the lower irradiance areas which are located directly above/centered on each LED/lens. Representative prints from the higher irradiance sites are shown in (a) and (d-f) – note the inside corners are fully bridged with cured resin. Representative prints from the lower irradiance sites are shown in (c) and (g-i) – note that the inside corners are not bridged with cured resin and have notable separation. These prints used 50 µm layer heights and 20 s layer exposure times.

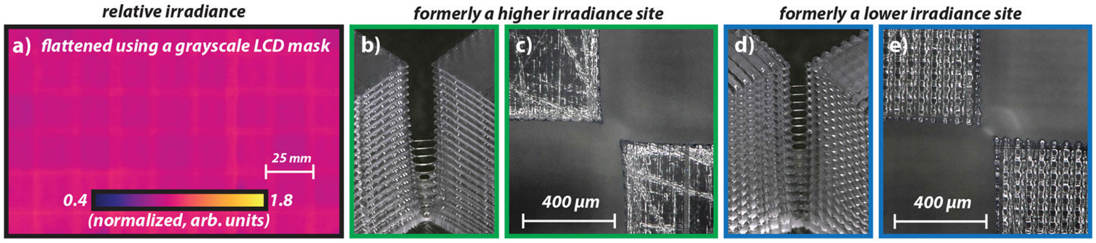

Figure 5:

(a) A map of the total irradiance (integration between 375 nm and 475 nm) normalized to the mean irradiance. Here, a grayscale mask was constructed and applied to the LCD in order to flatten the irradiance map. (b-c) A 45° view and top-down view of a representative ‘inside corner’ print from the formerly higher irradiance sites. (d-e) A 45° view and top-down view of a representative ‘inside corner’ print from the formerly lower irradiance sites. Note that after flattening the irradiance map using a grayscale mask, the overall inside corner profile between the sites is much more similar, but the surface texture is still quite different. These prints used a 50 μm layer heights and 36 s layer exposure times.

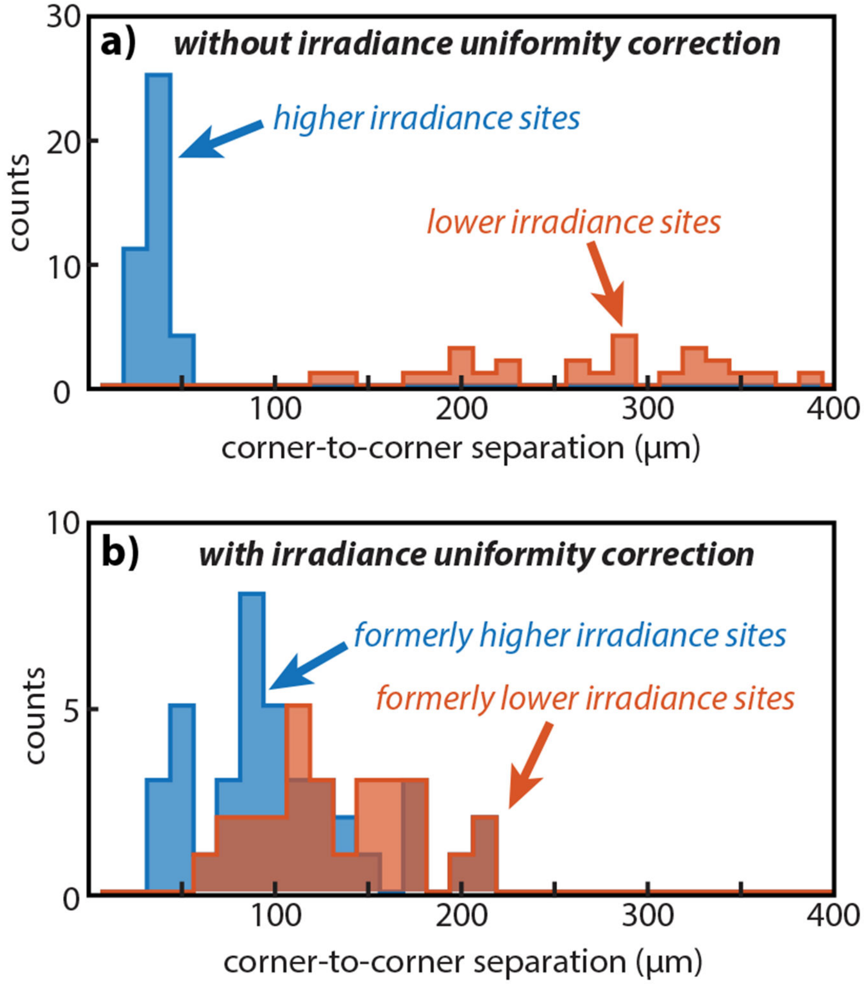

Figure 6:

(a) A histogram of the final layer corner-to-corner separation distance for all 68 test parts. Here, no grayscale uniformity correction mask was applied. The measured distribution of separation distances is non-overlapping between the higher and lower irradiance sites. (b) A histogram of the final layer corner-to-corner separation distance for all 68 test parts which were printed using a grayscale irradiance uniformity correction mask. Here, the two sets of sites yield distance distributions that have notable overlap. Note that in both (a) and (b) there is an approximately 50 μm uncertainty in the distance measurements due to the complex shape of these parts.

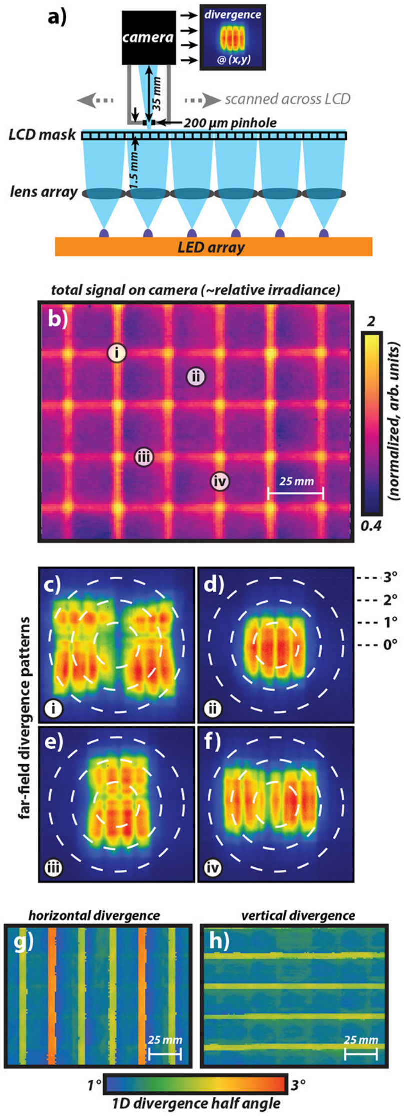

Figure 7:

(a) Measurement schematic for spatially mapping the divergence of the UV light transmitted through the LCD. A pinhole camera was rastered across the LCD surface while collecting spectra. (b) A map of the total signal on the camera (roughly corresponding to the irradiance) normalized to the mean signal. (c-f) Individual divergence patterns from the four locations indicated. (g-h) Spatial maps of the vertical and horizontal divergence. The specified divergence is given as the half angle associated with the fwhm of a vertical and horizontal 1-dimensional profiles.

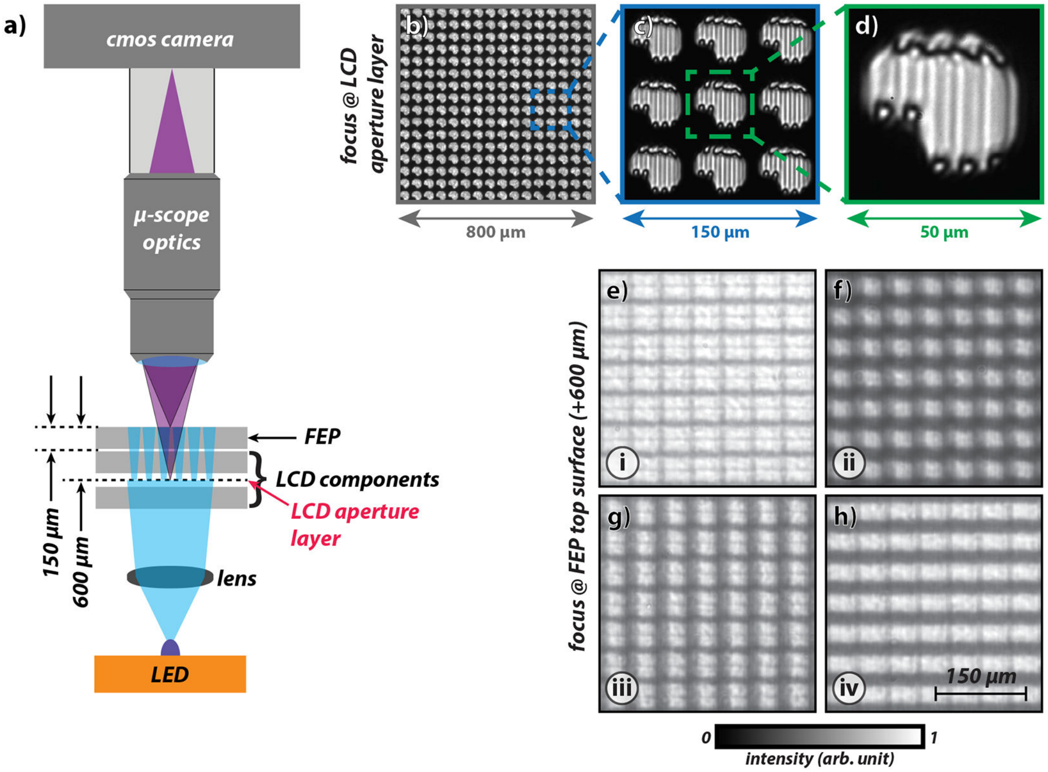

Figure 8:

(a) Measurement schematic for capturing images of the UV light being transmitted through the LCD pixels. (b-d) Images collected when the microscope is focused such that the pixels appear optimally focused. (e-h) Images collected at the locations specified in Fig. 7b when the microscope focus is shifted *ca.* $\Delta z = 600$ μm – *i.e.*, where the FEP/resin would typically be placed. For these latter images, it was ensured that the NA of the optical system was sufficient to prevent clipping of the light rays. Additionally, the same exposure and image processing was applied to each of the four images such that the intensity can be compared. Finally, note that no correction mask was applied during the collection of this data.

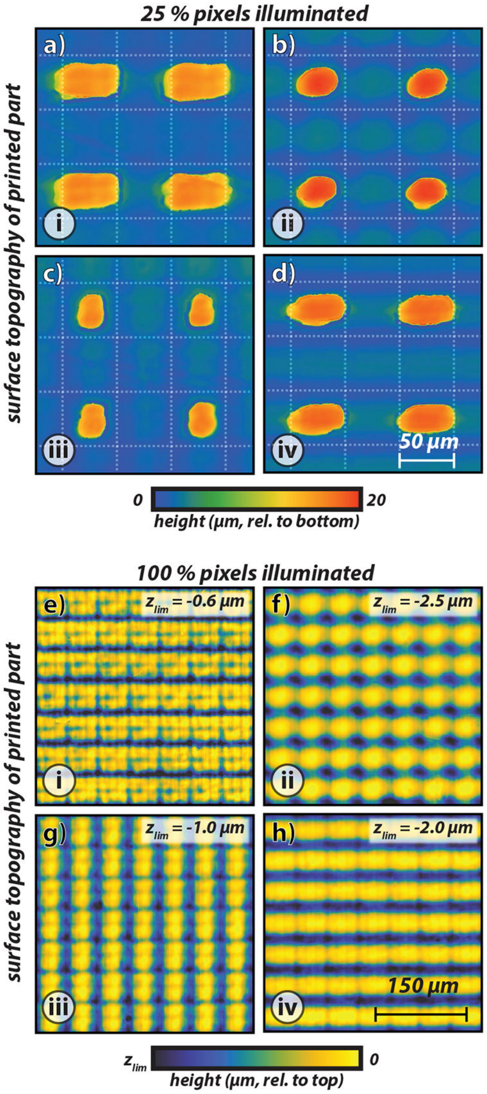

Figure 9:

(a-d) Laser scanning confocal microscope height map from the four locations specified in Fig. 7b for a sample where the final layer had every other pixel illuminated. The underlying layers had all pixels illuminated to serve as a flat background from which the height measurement is reference. The layer height was set to 20 µm. (e-h) Laser scanning confocal microscope height map from the four locations specified in Fig. 7b for a sample where the final layer (and all previous layers) had all pixels illuminated. The layer height was set to 50 µm. The height measurement is referenced to the highest pixels in the map. Both sets of samples were printing using the same correction mask as used in Fig. 5a to give a flattened irradiance map.